PHYSICAL REVIEW B **79**, 075435 (2009)

Electronic, structural, and transport properties of Ni-doped graphene nanoribbons

V. A. Rigo,[1,2] T. B. Martins,[1] Antonio J. R. da Silva,[1] A. Fazzio,[1,3] and R. H. Miwa[4]
[1]*Instituto de Física, Universidade de São Paulo, C. P. 66318, 05315-970 São Paulo, SP, Brazil*
[2]*Departamento de Física, Universidade Federal de Santa Maria, 97105-900 Santa Maria, RS, Brazil*
[3]*Centro de Ciências Naturais e Humanas, Universidade Federal do ABC, Santo André, SP, Brazil 09090-400*
[4]*Instituto de Física, Universidade Federal de Uberlândia, C.P. 593, 38400-902 Uberlândia, MG, Brazil*

(Received 24 June 2008; revised manuscript received 11 November 2008; published 20 February 2009)

We have investigated the electronic and transport properties of zigzag Ni-adsorbed graphene nanoribbons (Ni/GNRs) using *ab initio* calculations. We find that the Ni adatoms lying along the edge of zigzag GNRs represent the energetically most stable configuration, with an energy difference of approximately 0.3 eV when compared to the adsorption in the middle of the ribbon. The carbon atoms at the ribbon edges still present nonzero magnetic moments as in the pristine GNR even though there is a quenching by a factor of almost five in the value of the local magnetic moments at the C atoms bonded to the Ni. This quenching decays relatively fast and at approximately 9 Å from the Ni adsorption site the magnetic moments have already values close to the pristine ribbon. At the opposite edge and at the central carbon atoms the changes in the magnetic moments are negligible. The energetic preference for the antiparallel alignment between the magnetization at the opposite edges of the ribbon is still maintained upon Ni adsorption. We find many Ni *d*-related states within an energy window of 1 eV above and below the Fermi energy, which gives rise to a spin-dependent charge transport. These results suggest the possibility of manufacturing spin devices based on GNRs doped with Ni atoms.

DOI: 10.1103/PhysRevB.79.075435 PACS number(s): 71.15.Mb, 71.15.Dx, 72.25.Ba

I. INTRODUCTION

Within the family of synthesized materials based solely on carbon, the graphene sheet has been the subject of a great deal of attention.[1,2] This is related to the many interesting physical and chemical properties of these structures. It is topologically a two-dimensional solid, where the electronic properties are ruled by π-electrons in a hexagonal lattice. Among these electronic properties, one that deserves special mention is the extremely high carrier mobility, related to the linear band dispersion around the Fermi point.[3] This makes this system interesting for possible applications in electronic devices.

More recently, ribbon structures of graphene have been synthesized.[4] Those graphene nanoribbons (GNRs) exhibit an average width of few nanometers and more than 500 nm in length. Such a quasi-one-dimensional structure will give rise to an electronic confinement along the ribbons. The electronic properties of the GNRs can be tailored in a suitable way by controlling the ribbon width. Furthermore, similar to nanowires where the surface effects are important for their electronic properties and the energetic stability of the wires, the atomic arrangement along the edges of the ribbons play an important role in GNRs.[5–7] This latter property allows the manipulation of the electronic characteristics and, thus, provide an additional degree of freedom to build-up nanodevices (based on GNRs) for a given specific application. Another possibility to alter their electronic properties is via the adsorption or doping by external atoms or molecules.[8–10] Recent theoretical studies have shown that it is possible to change the transport properties of these ribbons, in particular, it is possible to create spin filters either by the application of electric fields[11] or by doping with atoms along the nanoribbon edges.[12,13] Those findings clearly place the graphene and the graphene nanoribbons as important materials addressing future applications in nanoelectronics. However, further investigations are necessary in order to improve our knowledge of the properties of graphene sheets and nanoribbons doped by external elements. In particular, we believe that transition metals (TMs) will play an interesting role on the electronic transport along GNRs.

Among the TMs, nickel atoms exhibit peculiar interactions with the graphene network. For instance, Ni acts as a catalytic metal for the growth of carbon nanotubes (CNTs) and carbon nanofibers (CNFs).[14,15] However, there are some controversies regarding the Ni adsorption sites on nanotubes. Based upon *ab initio* calculations, Yagi *et al.*[16] obtained the atop site as the energetically most favorable one for Ni adatoms on (4,4) single-walled CNTs. In contrast, on (8,0) single-walled CNTs, *ab initio* calculations performed by Durgun *et al.*[17] indicate that a Ni adatom lying on the bridge site (over a C–C bond) is the most likely configuration. During the CNT growth process, the temperature promotes the Ni diffusion on the tube surface and the Ni migrates toward the edge sites. In a very comprehensive total-energy investigation, Lee *et al.*[18] examined the catalytic mechanism of Ni atoms during the CNT growth process. In graphene sheets the Ni adatoms exhibit an energetic preference for the hole sites.[16,19] Further recent experimental investigations indicate the presence of Ni atoms occupying a carbon site within the graphene lattice.[20] Clearly, the presence of edges with different geometries will change not only the energetic picture of Ni adatoms on the graphene network but also the electronic and the magnetic properties (for the zigzag edges) of the GNRs.

Motivated by those experimental and theoretical findings, in this paper we examine the adsorption process of Ni adatom on the zigzag edge GNRs. Our total-energy results indicate that the Ni adatoms are most stable along the edge sites of the ribbon. The presence of Ni adatoms partially reduces the magnetic moment of the zigzag GNRs and induces a number of impurity states within the energy-band gap. The calculated electronic transmittance along the GNRs reveals a spin-dependent scattering process, suggesting the possibility to build up spin filters based upon graphene nanoribbons.

II. METHOD OF CALCULATION

All the electronic structure calculations were performed using total-energy density-functional theory (DFT),[21,22] using a localized atomic orbital basis set (LCAO) as implemented in the SIESTA code.[23] The generalized gradient approximation of Perdew, Burke and Ernzerhof (PBE-GGA) (Ref. 24) was used for the exchange-correlation (xc) term, and the atomic-ion core is described by Troullier-Martins pseudopotentials.[25] Nonlinear core correction[26] was used for Ni due to the overlap between the core and valence states. We used a double-ζ basis with polarization orbitals (DZP) for all the atoms, a 0.1 (for C and H) and 0.03 eV (for Ni) energy shift, and a real-space grid cutoff of 400 Ry.

A (5,0) zigzag GNR with three unit cells $[(\mathrm{GNR})_3]$ was used in a supercell approximation (total length of 7.482 Å) to perform all the initial Ni adsorption studies, with 36 C atoms and 6 H atoms plus the Ni atom. After the geometry relaxations and binding-energy calculations, the most stable Ni position was investigated both in the GNR ferro-*F* and GNR ferro-*A* edge spin configurations,[12,27] using now a nine unit-cell supercell $[(\mathrm{GNR})_9$; total length of 22.45 Å].

A 15 Monkhorst-Pack *k* grid was used along the $(\mathrm{GNR})_3$ growth direction and 6 for the $(\mathrm{GNR})_9$ for the Brillouin-zone integration. The structures were relaxed until the forces were smaller than 0.02 eV/Å.

The adsorption energy of Ni adatoms on the GNR (E^{ads}) can be written as

$$E^{\mathrm{ads}} = E[\mathrm{Ni/GNR}] - E[\mathrm{GNR}] - E[\mathrm{Ni}],$$

where $E[\mathrm{Ni/GNR}]$ and $E[\mathrm{GNR}]$ represent the total energies of the Ni-adsorbed and pristine ferro-*A* GNRs, respectively, and $E[\mathrm{Ni}]$ is the total energy of an isolated Ni atom in a high spin configuration.

To obtain the transport properties of these systems the procedure initially devised by Caroli *et al.*[28] is employed, where the system is divided into three parts: two electrodes, left (L) and right (R), and a scattering region (M). The electrodes were taken as two semi-infinite metallic GNR, and the scattering region is described by five unit cells of (5,0) GNR (region where the atoms were relaxed) plus three unit cells (coupling regions) on each side [fixed in the geometry of the pristine (5,0) GNR, see Fig. 1]. This size is enough to guarantee that (i) there is no interaction between the two leads; (ii) the Hamiltonian matrix elements have converged to the bulk [pristine (5,0) GNR] values at the edges of the cell; (iii) the coupling to the electrodes is via bulklike matrix elements. The fundamental theory of nonequilibrium Green's functions[29] is used to obtain the transport properties of a scattering atomistic system coupled to electrodes.[30] The Hamiltonian of the scattering region is approximated by the Kohn-Sham Hamiltonian[22] from density-functional theory calculations,[31] as implemented in the TRANSAMPA code; see Ref. 36 for details.

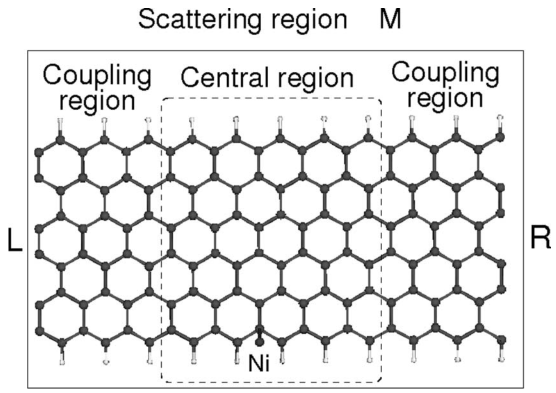

FIG. 1. Geometric structure for transport calculations. The scattering region (m) is divided into three parts: the left and right electrode coupling regions and the central region (inside the dashed line). The Ni atom in the most stable adsorption site is shown.

Briefly, to obtain the conductance of the system, the central quantity is the Green's function, at the energy E, of the scattering region,

$$G_M(E) = [ES_M - H_M - \Sigma_L(E) - \Sigma_R(E)]^{-1}, \tag{1}$$

where H_M and S_M are the Hamiltonian and overlap matrices for the scattering region and $\Sigma_L(E)[\Sigma_R(E)]$ is the self-energy for the left-hand (right-hand) side electrode. Finally, the transmittance can be obtained from a Buttiker-Landauer-type equation,

$$T(E) = \mathrm{Tr}\{\Gamma_L G_M^{\dagger} \Gamma_R G_M\}, \tag{2}$$

where $\Gamma_{L(R)} = i[\Sigma_{L(R)} - \Sigma_{L(R)}^{\dagger}]$ represents the coupling to the electrodes. In order to have metallic leads, we have considered the ferro-*F* spin configuration, cf. Figs. 2(b) and 9(d), in all transport calculations.

III. RESULTS AND DISCUSSION

We initially considered the pristine (5,0) GNR. As discussed previously in the literature, the edges of a hydrogenated GNR tend to become spin polarized, inducing an overall nonzero local magnetization.[37] In Fig. 2 we present two stable spin-density configurations for the hydrogenated (5,0) GNR, viz.: ferro-*A* [Fig. 2(a)] and ferro-*F* [Fig. 2(b)]. The local spin density $\sigma(\mathbf{r})$ was calculated as the difference between the up-spin and down-spin densities, $\rho_{\uparrow}(\mathbf{r})$ and $\rho_{\downarrow}(\mathbf{r})$, respectively, i.e., $\sigma(\mathbf{r}) = \rho_{\uparrow}(\mathbf{r}) - \rho_{\downarrow}(\mathbf{r})$. The ferro-*A* configuration has the spin densities of the two edges aligned in an antiparallel fashion, whereas in the ferro-*F* they are aligned in a parallel configuration. As can be seen, in the ferro-*A* there is a ferromagnetic ordering within a given carbon sublattice, and antiferromagnetic ordering between the two carbon sublattices. As the carbon atoms at the opposed edges belong to distinct sublattices, there is no frustration in the ferro-*A* configuration. However, as in ferro-*F* the two edges have the same spin alignment, this induces a frustration in the system, reflected by a *wall* in the middle of the ribbon

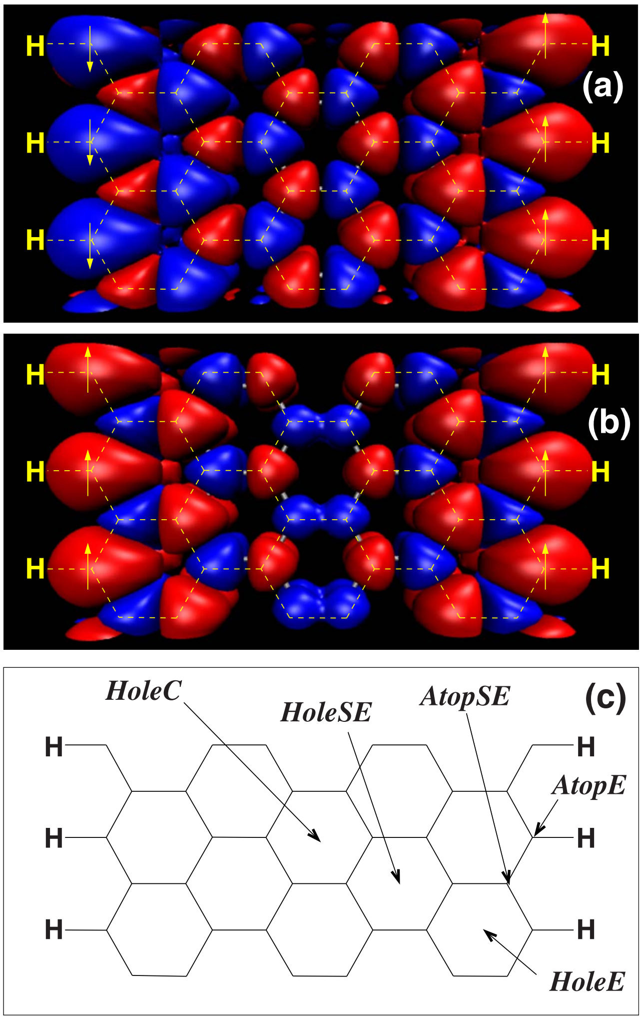

FIG. 2. (Color online) (a) ferro-*A* and (b) ferro-*F* spin-density distribution $\sigma(\mathbf{r})=\rho_{\uparrow}(\mathbf{r})-\rho_{\downarrow}(\mathbf{r})$ along the hydrogenated (5,0) GNR. Red (light grey) indicates positive values (net spin up), whereas blue (dark grey) indicates negative values (net spin down). (c) Ni adsorption positions, atop and hole, at the: center (*C*), edge (*E*), and subedge (SE) sites, on the (5,0) GNR were investigated in the present work.

where the spins of nearest-neighbor carbon atoms have parallel alignment. As the nearest-neighbor atoms belong to distinct sublattices this parallel alignment increases the energy of the ferro-*F* configuration as compared to the ferro-*A*.[12,37] We find a total-energy difference of 12 meV/unit cell. It has been previously shown[38] that use of distinct xc-functionals can affect details of the GNR magnetic configuration, such as the value of the local magnetic moments and the ferro-*F*-ferro-*A* energy difference. However, as the same authors' report, the qualitative features of the results are robust with respect to the differing treatments of xc-functionals.[38] This same conclusion should hold for the results of Ni-doped GNRs presented below. We note that for both configurations, ferro-*A* and ferro-*F*, the spin-density distributions along the ribbon edges and at the atoms close to the edges have absolute values that are very similar. The major differences are close to the middle of the ribbon, where the frustration in the ferro-*F* configuration imposes the spin reversal.

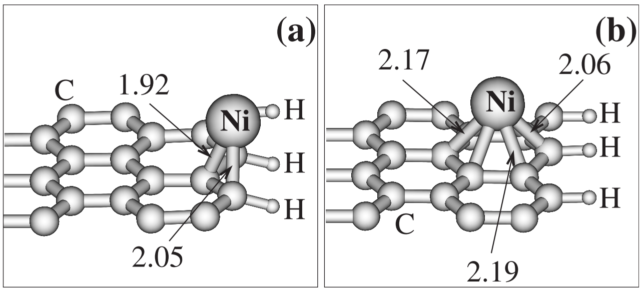

FIG. 3. Equilibrium geometries of (a) atop SE and (b) hole *E* geometries for Ni adatoms on the (5,0) GNR. The atomic distances are in angstrom.

These spin-density distributions of pristine GNR may change upon adsorption of foreign atoms. Figure 2(c) presents the Ni adsorption sites on the (5,0) GNR that were investigated in the present work. Bridge sites were unstable. The equilibrium geometries of atop *SE* and hole *E* structures are depicted in Figs. 3(a) and 3(b), respectively. The Ni adatom is three (six) fold coordinated on atop *SE* (hole *E*), with Ni-C bond lengths of 1.9–2.1 Å(2.0–2.2 Å).

Our calculated adsorption energies, summarized in Table I, indicate an energetic preference of about 30 meV for the ferro-*A* spin-density configuration. For the atop *E* structure, however, the ferro-*F* configuration was unstable, and converged to the ferro-*A*. The similarity between the energy difference between ferro-*F* and ferro-*A* configurations with (≃30 meV) and without (≃36 meV) adsorbed Ni atoms suggests that the spin arrangement of the carbon atoms in the middle of the ribbon is maintained after Ni adsorption (note that the reference for the adsorption energies is always the ferro-*A* configuration; this implies that the Ni binding energies in both the ferro-*A* and ferro-*F* configurations are similar). Indeed the statement above is supported by the calculation of the magnetic moments at the carbon atoms in a chain (similar to a primitive unit cell of a pristine ribbon) perpendicular to the GNR growth direction that contain the Ni atom, as presented in Fig. 4 and by the inspection of the spin-density arrangement for all configurations.

Figure 4 presents the local magnetic moment of the carbons atoms along a perpendicular cross section of the GNR unit cell that passes through Ni atom for the most stable atop *SE* geometry in the ferro-*F* configuration. The plot starts from the GNR edge closer to the Ni adatom and goes along the *x* direction (cross section of the GNR growth direction). We can see that neither the net magnetization in the middle of the GNR changed significantly nor the Ni perturbation affected the opposite edge. A similar ferro-*A* energy preference and magnetization were found when the Ni was on the GNR hole *C* configuration.

TABLE I. Adsorption energy (E^{ads}), for the ferro-*F* and ferro-(*A*) configurations, of Ni adatoms on (5,0) hydrogenated GNR.

Config.	Atop SE	Hole *E*	Atop *E*	Hole SE	Hole *C*
Ferro-*A*	−2.21	−2.17	−1.98	−1.95	−1.92
Ferro-*F*	−2.17	−2.14	Unstable	−1.92	−1.89

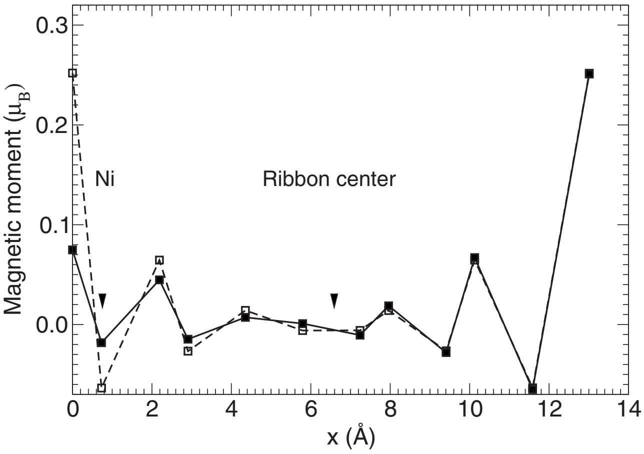

FIG. 4. Net magnetization along a cross section of the ribbon unit cell passing through the carbon atoms and the Ni atom for the ferro-*F* configuration. Atoms of the pristine (dashed line) and the Ni-adsorbed atop SE structure (solid line) are shown.

For Ni adatoms on graphene sheets we find that hole sites (similar to hole *C* in the nanoribbon) represent the energetically most stable configuration. In graphene we obtained $E^{\text{ads}}=-1.76$ and -1.31 eV for hole and atop geometries, respectively. This energy difference between hole and atop geometries is very close to previous calculations.[19] Further *ab initio* calculations performed by Yagi *et al.*[16] indicated an energetic preference for the hole structure for Ni adatoms on graphene sheet as well ($E^{\text{ads}}=-1.53$ eV), whereas on the (4,4) CNT the Ni adsorption on top of the carbon atoms becomes energetically more favorable with $E^{\text{ads}}=-2.00$ eV. Those results indicate that the geometry of the graphene network, namely, ribbons, sheets, and nanotubes, play an important role for the Ni adsorption process. Thus, based upon our total energy results, we expect a higher concentration of Ni adatoms lying along the edges of GNRs, for instance, the atop *SE* and hole *E* configurations. Indeed, the tendency of Ni adatoms to segregate toward the nanoribbon edge, given by the energy difference between the adsorption in the middle and at the edge of the GNR, supports the catalytic growth model, proposed by Lee *et al.*,[18] for single-walled carbon nanotubes.

Figures 5(a) and 5(b) present the total charge density $\rho(\mathbf{r})$ along the Ni-C bonds perpendicular to the growth direction for the energetically stable atop *SE* and hole *E* configurations, respectively. The total charge density $\rho(\mathbf{r})$ was calculated as the sum between the up-spin and down-spin densities, i.e., $\rho(\mathbf{r})=\rho_{\uparrow}(\mathbf{r})+\rho_{\downarrow}(\mathbf{r})$. Those diagrams indicate the formation of Ni-C covalent bonds.

Figure 6 presents the projected density of states (PDOS) for some Ni-adsorbed configurations on the GNR. We observe that the occupied 4*s* and 3*d* orbitals of Ni adatoms are localized within an energy range of ~2 eV below the Fermi level. For an isolated Ni atom, the ground-state configuration is $4s^2 3d^8$, where these 4*s* and 3*d* orbitals are very close in energy. Upon the formation of Ni-C bonds, mostly a $4s \rightarrow 3d$ electronic charge transfer takes place. For the energetically most stable atop *SE* structure we find the following electronic occupation, $4s^{0.5}4p^{0.2}3d^{8.7}$ by means of PDOS integration.[39] The PDOS of the atop *SE* configuration, depicted in Fig. 6(a), indicates that the 4*s* empty states lie within an energy interval of 1 eV above the Fermi level (being resonant in the conduction band of the GNR), whereas the 3*d* orbitals of the Ni adatom hybridize with the nearest-neighbor C 2*p* orbitals.

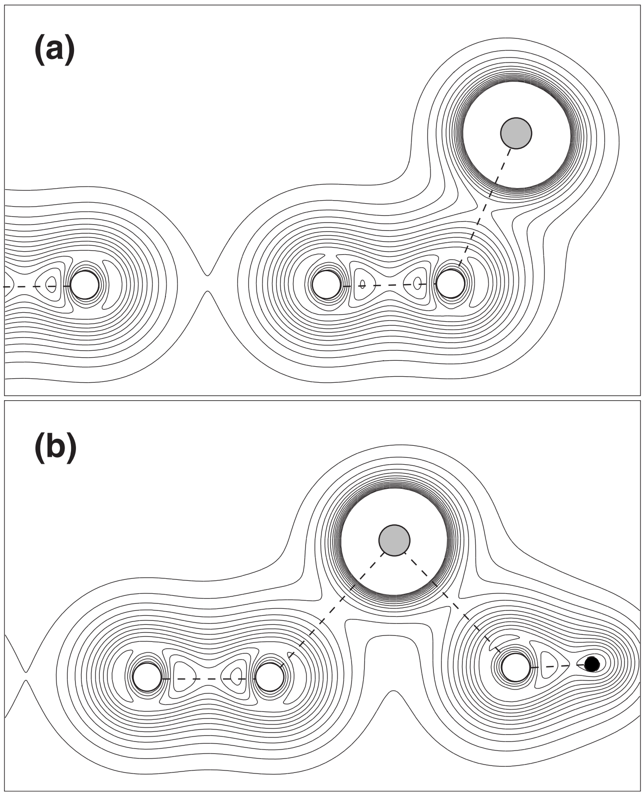

FIG. 5. Total charge density along the Ni-C bonds for the (a) atop SE and (b) hole *E* configurations. The cross section is perpendicular to the GNR growth direction.

The occupied Ni 3*d* orbitals spread through an energy window of approximately 2 eV within the GNR valence band, whereas the 4*s* states present relatively narrow peaks within ≃1 eV above the Fermi energy.

In Figs. 6(b) and 6(c) we present the Ni PDOS for the hole *E* and atop *E*, configurations, respectively. Those PDOS diagrams reveal the following aspects: (i) the hybridization between Ni 3*d* and the carbon 2*p* orbitals, and (ii) the Ni →GNR charge transfer increase with the coordination number of Ni adatoms. In addition, 3*d* peaks for the atop *E* structure are narrower when compared to the 3*d* peaks for the atop *SE* and hole *E* configurations, indicating a smaller hybridization. Also, from the PDOS for the hole *E* structure (the Ni adatom is sixfold coordinated) the hybridization of 3*d* states seems to be more intense when compared with atop *SE*, and the electronic occupation of the 4*p* orbital is the largest one (even though the $4s \rightarrow 4p$ charge transfer is quite small in all cases). The electronic configuration of the hole *E* Ni adatoms is $4s^{0.2}4p^{0.3}3d^{8.7}$. In contrast, for the atop *E* structure, where the Ni adatom forms a single Ni-C bond, we obtained the following Ni electronic distribution $4s^{1.0}4p^{0.1}3d^{8.6}$, having the largest 4*s* occupation.

Table II summarizes the atomic population and the net magnetic moments obtained from the Ni PDOS for the atop

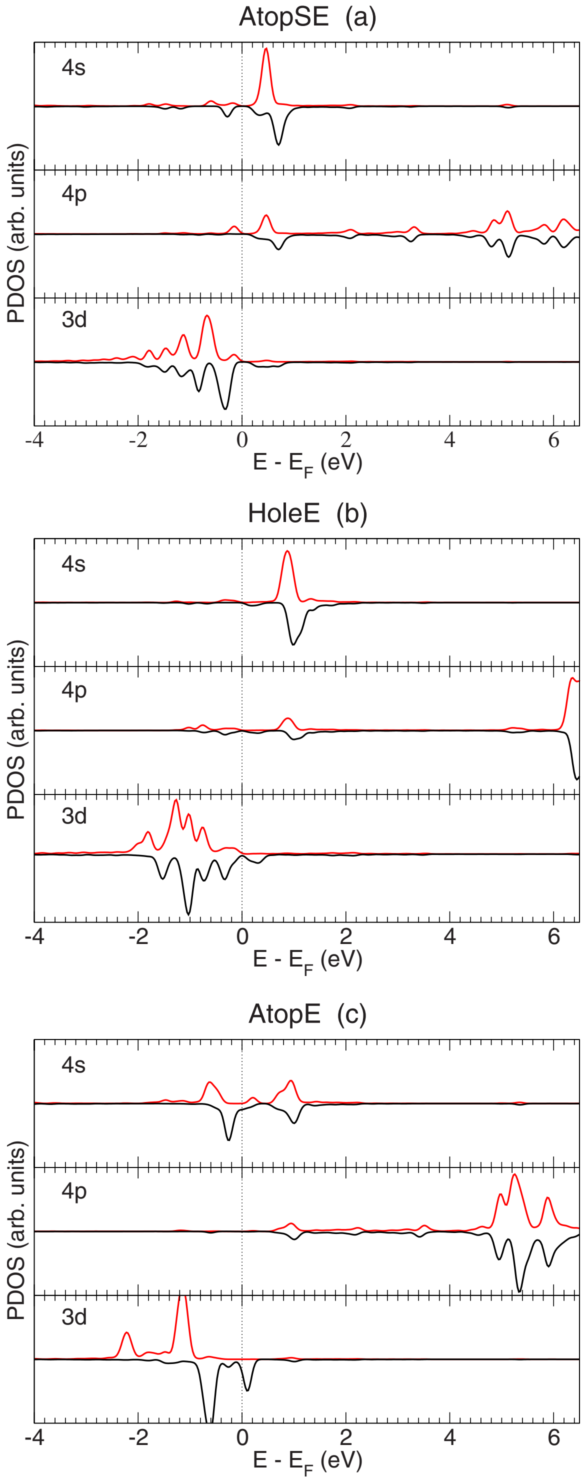

FIG. 6. (Color online) PDOSs of 4s, 4p, and 3d Ni orbitals for the atop SE (top), hole E (center), and atop E (bottom) configurations. The vertical dotted lines at zero correspond to the Fermi energy.

SE, hole E configurations, and atop E which are sixfold, threefold, and onefold coordinated, respectively, on the ferro-A GNR. Similar results were obtained for Ni adatoms on ferro-F GNR. The magnetic moments of Ni adatoms are correlated with the hybridization of Ni 3d orbitals, which is (as we observed above) proportional to the coordination of Ni adatoms. For the energetically most favorable structure, atop *SE*, we find magnetic moments of $0.53\mu_B$ and $0.47\mu_B$ for Ni adatoms on ferro-A and ferro-F GNRs, respectively. The sixfold-coordinated Ni adatom (hole E structure) exhibits the lowest net magnetization, $0.46\mu_B$ and $0.43\mu_B$ for the ferro-A and ferro-F GNRs, respectively. Indeed, the magnetic moments of Ni atoms (at hole sites) become almost negligible as the adsorption site moves toward the center of the ribbon, which is similar to what we observe for Ni adatoms on graphene sheets. On graphene sheets, the magnetic moment of TM adatoms reduces by about $2\mu_B$ with respect to the free-atom configuration.[16,19,42] On the other hand, in atop E the Ni adatom exhibits a net magnetization of $0.90\mu_B$ and $0.97\mu_B$ on the ferro-A and ferro-F GNRs, respectively. For both systems, the contribution of 4s and 4p orbitals to the Ni magnetic moment are quite small when compared to the 3d orbitals.

TABLE II. Atomic orbital occupation and the local magnetic moment (in μ_B units) of Ni adatoms for the atop SE, hole E, and atop E configurations on the ferro-A GNR. The parentheses indicates the coordination number to Ni in each geometry.

Config.	Atop SE (3)	Hole E (6)	Atop E (1)
		Occupation	
4s	0.5	0.2	1.0
3d	8.7	8.7	8.6
		Magnetization	
4s	−0.01	0.03	−0.02
3d	0.45	0.39	0.94
Total	0.53	0.46	0.90

Figures 7(a) and 7(b) present the spin-density distribution for the atop *SE* ferro-A and ferro-F model, respectively. In those diagrams we find that the local magnetization along the GNR edge where Ni is substituted, increases upon Ni adsorption. However, along the inner sites of the GNR the spin-density distributions are different for Ni adatoms adsorbed on ferro-A and ferro-F GNRs. Comparing with the respective pristine systems, we observe that the ferro-A structure is less perturbed upon Ni adsorption than the ferro-F system, see Figs. 7(a) and 7(b), respectively. Indeed, the spin-density configuration at the inner sites of atop *SE* ferro-A, depicted in Fig. 7(a), resembles the one for the pristine ferro-A GNR [Fig. 2(a)]. Thus, it suggests that, similarly to the pristine systems, the energetic preference of the ferro-A configuration (see Table I) is ruled by an energetically favorable spin-density distribution along the inner sites of the GNR.

The magnetization in the GNR atoms are locally reduced upon Ni adsorption. The weak Ni effect in the middle of the ferro-F atop *SE* GNR was shown in Fig. 4, and the energetic preference for the ferro-A spin-density configuration was maintained. However in the carbon atoms close to the GNR edge the magnetic-moment reduction is more pronounced. In Fig. 8 we present the net magnetization of the edge and subedge carbon atoms for the atop *SE* structure. In this case, we have increased the length of our supercell to nine (5,0)

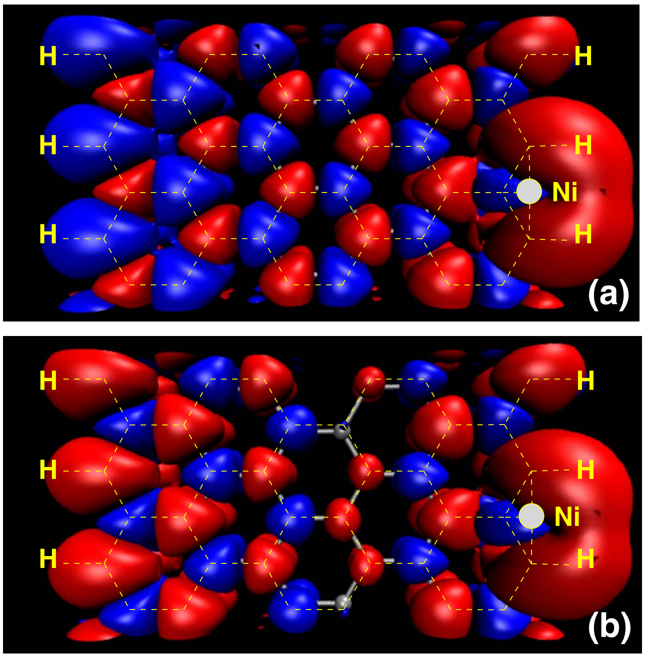

FIG. 7. (Color online) Spin-density distribution for the atop SE configuration in the (a) ferro-*A* and (b) ferro-*F* GNRs.

units along the nanoribbon growth direction (z). The dashed lines represent the magnetization of the pristine system and the Ni position in the doped GNR is indicated. This diagram reveals that the magnetizations along edge and subedge carbon atoms are locally reduced upon the Ni adsorption. For the atop *SE* configuration, the edge (subedge) C atoms are coupled antiferromagnetically (ferromagnetically) to the Ni adatoms.

The π/π^* electronic states give rise to flat energy bands near the Fermi level for the pristine ferro-*A* [Fig. 9(a)] and ferro-*F* [Fig. 9(d)] GNRs, which are related to edge states. The former structure is semiconducting, whereas the ferro-*F* system is metallic.[12,27,37] We verify that this electronic character of the GNR does not change upon Ni adsorption. The ferro-*A* atop *SE* structure [Fig. 9(b)] maintains the semiconducting character, however, the energy bands become nondegenerate. The spin-down energy bands (dashed dark lines) near the fundamental gap are perturbed by the presence of Ni adatoms. On the other hand, the highest occupied and the lowest unoccupied spin-up energy bands (solid red lines), related to the edge opposite to the Ni adsorption site, are less perturbed. Similarly, for the hole *E* configuration, the spin-down energy bands interact with the electronic states of Ni adatoms, whereas the spin-up bands somewhat maintain the original form of the pristine ferro-*A* GNR. Figures 9(e) and 9(f) show that the spin-up and spin-down bands crossing point at the Fermi level has been maintained for the Ni adsorbed ferro-*F* GNR. Although energetically less favorable than atop *SE* and hole *E*, the calculated electronic band structure of atop *E* indicates the formation of a half-metallic band structure (not shown).

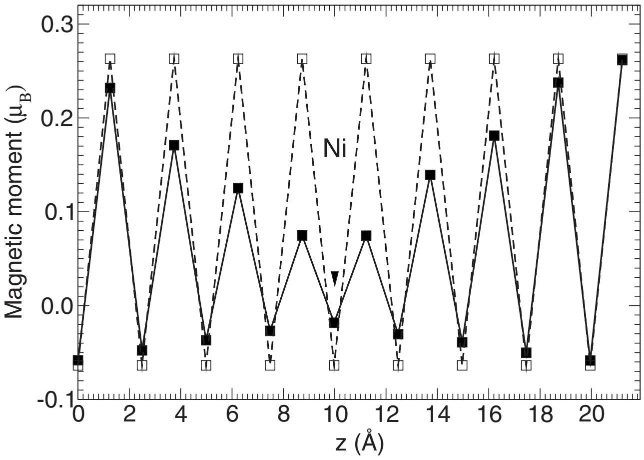

FIG. 8. Net magnetization along the edge and subedge carbon atoms of the pristine (dashed line) and the Ni-adsorbed ferro- *F*, atop SE structure (solid line).

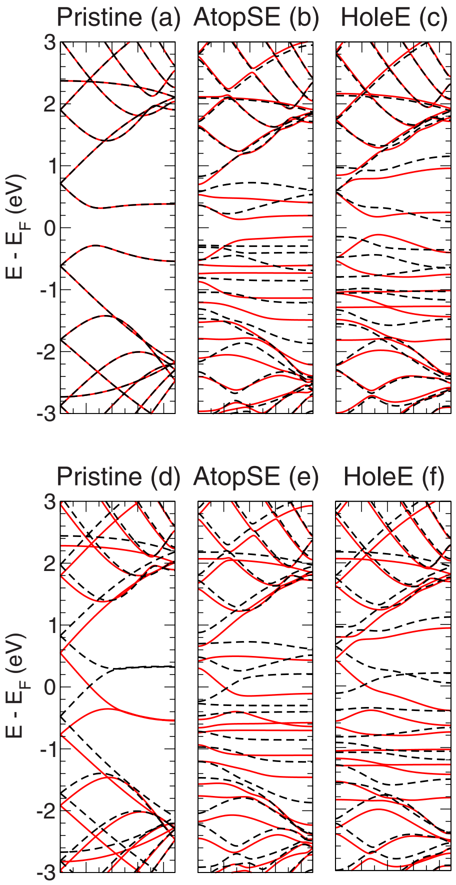

FIG. 9. (Color online) Electronic band structure of [(a)–(c)] ferro-*A* and [(d)–(f)] ferro-*F* (5,0) GNR. [(a) and (d)] Pristine GNR, [(b) and (e)] Ni-adsorbed atop SE, and [(c) and (f)] hole *E* configurations. The red full lines correspond to up-spin and dark dashed lines correspond to down-spin.

The electronic band diagrams presented in Fig. 9 clearly indicate that the electronic perturbations due to the presence of Ni adatoms are mostly localized within an energy interval of ±2 eV relative to the Fermi level, which is expected from the PDOS results presented in Fig. 6. The localized 3d states near the Fermi level due to the impurity atom (Ni) will play an important role for the electronic transport along the GNR.

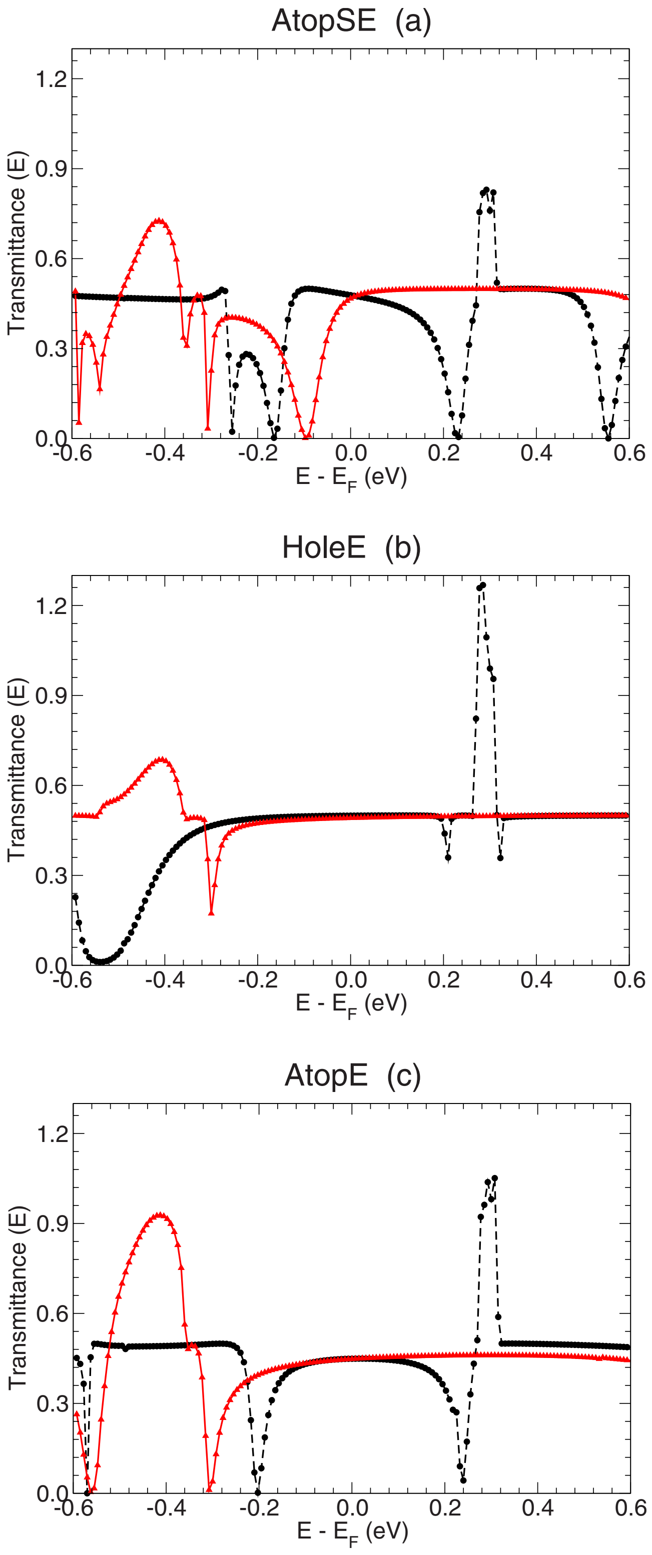

FIG. 10. (Color online) Spin-dependent electronic transmittance for the (a) atop SE, (b) hole *E*, and (c) atop *E* configurations. The red full (triangle up) lines are for the up transmittance channels and dashed dark (circle) lines refer to the down transmittance channel.

Indeed, we find a number of drops in the transmittance that can be correlated with the presence of Ni states in this energy window.

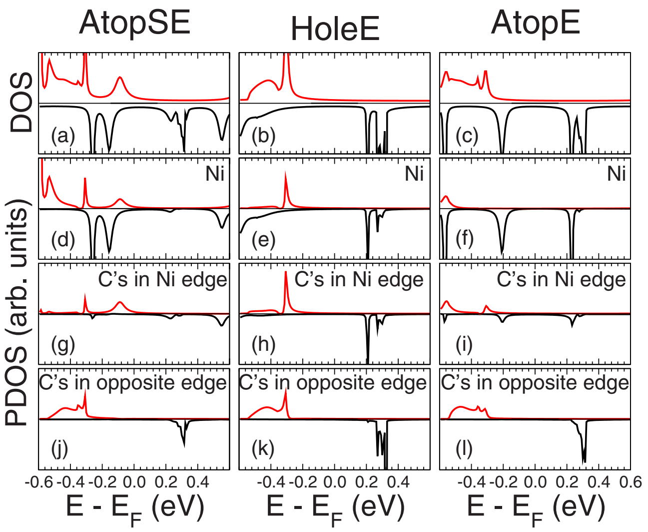

FIG. 11. (Color online) Total DOS for (a) atop SE, (b) hole *E*, and (c) atop *E* configurations. PDOS for: Ni in (d) atop SE, (e) hole *E*, and (f) atop *E*; carbon atoms at the edge where the Ni is adsorbed in Fig. 1 (C's in Ni edge) for (g) atop SE, (h) hole *E*, and (i) atop *E*; carbon atoms at the opposite edge from the Ni-adsorbed site in Fig. 1 (C's in opposite edge) for (j) atop SE, (k) hole *E*, and (l) atop *E*.

For the transmittance ($T^{\sigma};\sigma=\uparrow,\downarrow$) calculations, we have considered the energetically most stable atop *SE*, hole *E*, and atop *E* configurations. Pristine ferro-*F* GNR presents a transmittance $T=0.5$, for each spin channel near the Fermi level, namely, $T^{\uparrow}(E)=T^{\downarrow}(E)=0.5$ for $E=E_F$. Figures 10(a)–10(c) show that upon Ni adsorption in the atop *SE*, hole *E*, and atop *E* configurations, the $T^{\uparrow}(E)$ and $T^{\downarrow}(E)$ spin degeneracy has been broken. Moreover, we observe many spin-dependent transmittance drops.

These drops can be attributed to the interaction between impurity-induced states and the propagating waves composed by the C $2p$ π/π^* orbitals along the GNR.[43–45] The position of the dips or peaks in the transmittances shown in Figs. 10(a)–10(c) are correlated with the peaks in the density of states (DOS). In Figs. 11(a)–11(c) we present the total DOS of the system calculated using Green's function[46] for the atop *SE*, hole *E*, and atop *E* geometries, respectively. To obtain the contribution of the Ni impurity and the edges states for the DOS, we calculated the PDOS also using the Green's function.[46] Figures 11(d)–11(f) show the Ni PDOS ($4sp$ and $3d$) for atop *SE*, hole *E*, and atop *E* geometries, respectively, whereas Figs. 11(g)–11(i) show the PDOS for the carbon atoms at the edge where the Ni is adsorbed in Fig. 1 (C's in Ni edge) for the atop *SE*, hole *E*, and atop *E* geometries. Finally, Figs. 11(j)–11(l) show the PDOS for the carbon atoms at the opposite edge from where the Ni is adsorbed (C's in opposite edge), also for the atop *SE*, hole *E*, and atop *E* geometries, respectively.

As can be seen from Fig. 10, all the transmittance curves have many structures. These are either large drops in the transmittances or peaks where the transmittances become larger than 0.5. These large variations occur in an energy window of ±0.6 eV from E_F. The drops can be correlated with Ni induced states and the peaks to edge-related states. For example, considering the atop *SE* configuration, it is possible to see from the Ni PDOS in Fig. 11(d) that for the up-spin there is a peak at approximately −0.08 eV below the Fermi energy and another one close to −0.3 eV. Due to the hybridization with the carbon atoms, these peaks also appear at the PDOS for the C atoms at the Ni edge. For the Ni spin-down states, there are two similar peaks between −0.1 and −0.24 eV. The manifestation of these state in the transport properties is an almost complete blocking of the transmittance at these energies. For the GNR considered the transmittance actually goes to zero at some points, but for larger GNR width this result might change. In any case, the important fact is that for some energies there will be a large spin current polarization, which could be used in spintronic devices. Similar results are also observed for the other Ni-adsorbed configurations. However, for the atop *SE* this effect happens closest to the Fermi energy, and the resonances are relatively narrow. For the hole *E*, where the hybridization is larger, the drops in transmittance are broader and they happen only farther away from E_F. Besides the transmittance drops, there are also peaks that occur for energies where there are edge-related states, as can be seen from Figs. 11(g)–11(l).

IV. SUMMARY

In summary, comparing the binding energies of Ni adatoms on GNRs, we find that Ni adatoms lying along the edge of zigzag GNRs represents the energetically most stable configuration, introducing many resonant peaks in the DOS within an energy interval of ±2 eV with respect to the Fermi level. Our calculated net magnetization indicates a decrease in the Ni magnetic moment compared to the isolated atom due to the formation of Ni-C bonds and a $4s \rightarrow 3d$ charge transfers. However, the presence of these impurity related levels changes the electronic transport properties along the GNRs, with quite different behavior for the spin-up and spin-down components. We find a number of transmittance drops for each spin channel attributed to the scattering processes between the propagating wave from the leads and the Ni-induced states near the Fermi level. Since the drops for each spin channel happen at distinct energies, our results suggest the possibility of tuning spin-polarized electronic transport on zigzag GNRs through a suitable doping process by Ni, and most likely by other transition metals as well.

ACKNOWLEDGMENTS

The authors acknowledge the support by Brazilian agencies CNPq, FAPESP, FAPEMIG and CAPES. This work was partially developed at CENAPAD/SP.

---

[1] K. S. Novoselov, D. Jiang, F. Schedin, T. J. Booth, V. V. Khotkevich, S. V. Morozov, and A. K. Geim, Proc. Natl. Acad. Sci. U.S.A. **102**, 10451 (2005).

[2] S. Stankovich, D. A. Dikin, G. H. B. Dommett, K. M. Kohlhaas, E. J. Zimney, E. A. Stach, R. D. Piner, S. T. Nguyen, and R. S. Ruoff, Nature (London) **442**, 282 (2006).

[3] K. S. Novoselov, A. K. Geim, S. V. Morozov, D. Jiang, M. I. Katsnelson, V. Grigoreva, S. V. Dubonos, and A. A. Firsov, Nature (London) **438**, 197 (2005).

[4] L. G. Cançado, M. A. Pimenta, B. R. A. Neves, G. Medeiros-Ribeiro, T. Enoki, Y. Kobayashi, K. Takai, K. I. Fukui, M. S. Dresselhaus, R. Saito, and A. Jorio, Phys. Rev. Lett. **93**, 047403 (2004).

[5] V. Barone, O. Hod, and G. E. Scuseria, Nano Lett. **6**, 2748 (2006).

[6] L. Pisani, J. A. Chan, B. Montanari, and N. M. Harrison, Phys. Rev. B **75**, 064418 (2007).

[7] T. Enoki, Y. Kobayashi, and K. I. Fukui, Int. Rev. Phys. Chem. **26**, 609 (2007).

[8] D.-e. Jiang, B. G. Sumpter, and S. Dai, J. Chem. Phys. **126**, 134701 (2007).

[9] O. Hod, V. Barone, J. E. Peralta, and G. Scuseria, Nano Lett. **7**, 2295 (2007).

[10] D. Gunlycke, J. Li, J. W. Mintmire, and C. T. White, Appl. Phys. Lett. **91**, 112108 (2007).

[11] Y.-W. Son, M. L. Cohen, and S. G. Louie, Nature (London) **444**, 347 (2006).

[12] T. B. Martins, R. H. Miwa, A. J. R. da Silva, and A. Fazzio, Phys. Rev. Lett. **98**, 196803 (2007).

[13] T. B. Martins, R. H. Miwa, A. J. R. da Silva, and A. Fazzio, Nano Lett. **8**, 2293 (2008).

[14] F. Banhart, J. C. Charlier, and P. M. Ajayan, Phys. Rev. Lett. **84**, 686 (2000).

[15] S. Helveg, C. Lopez-Cartes, J. Sehested, P. L. Hansen, B. S. Clausen, J. R. Rostrup-Nilsen, F. Abild-Pedersen, and J. K. Norskov, Nature (London) **427**, 426 (2004).

[16] Y. Yagi, T. M. Briere, M. H. F. Sluiter, V. Kumar, A. A. Farajian, and Y. Kawazoe, Phys. Rev. B **69**, 075414 (2004).

[17] E. Durgun, S. Dag, V. M. K. Bagci, O. Gulseren, T. Yildirim, and S. Ciraci, Phys. Rev. B **67**, 201401(R) (2003).

[18] Y. H. Lee, S. G. Kim, and D. Tománek, Phys. Rev. Lett. **78**, 2393 (1997).

[19] D. M. Duffy and J. A. Blackman, Phys. Rev. B **58**, 7443 (1998).

[20] M. Ushiro, K. Uno, T. Fujikawa, Y. Sato, K. Tohji, F. Watari, W.-J. Chun, Y. Koike, and K. Asakura, Phys. Rev. B **73**, 144103 (2006).

[21] P. Hohenberg and W. Kohn, Phys. Rev. **136**, B864 (1964).

[22] W. Kohn and L. J. Sham, Phys. Rev. **140**, A1133 (1965).

[23] J. M. Soler, E. Artacho, J. D. Gale, A. García, J. Junquera, P. Ordejón, and D. Sánchez-Portal, J. Phys.: Condens. Matter **14**, 2745 (2002).

[24] J. P. Perdew, K. Burke, and M. Ernzerhof, Phys. Rev. Lett. **77**, 3865 (1996).

[25] N. Troullier and J. L. Martins, Phys. Rev. B **43**, 1993 (1991).

[26] S. G. Louie, S. Froyen, and M. L. Cohen, Phys. Rev. B **26**, 1738 (1982).

[27] Y.-W. Son, M. L. Cohen, and S. G. Louie, Phys. Rev. Lett. **97**, 216803 (2006).

[28] C. Caroli, R. Combescot, P. Nozieres, and D. Saint-James, J. Phys. C **4**, 916 (1971).

[29] L. V. Keldysh, Sov. Phys. JETP **20**, 1018 (1965); L. P. Kadanoff and G. Baym, *Quantum Statistical Mechanics* (Benjamin, Menlo Park, 1962).

[30] Y. Meir and N. S. Wingreen, Phys. Rev. Lett. **68**, 2512 (1992).

[31] The use of DFT to describe the quasiparticle spectra suffers from the intrinsic errors associated with the position of the Kohn-Sham eigenvalues (Refs. 32 and 33), which can be largely associated with the self-interaction error (SIE) present in the local or semilocal exchange and correlation functionals (Ref. 34), such as PBE which employed in the present work. However, this issue is more important for systems where the scattering region is weakly coupled to the electrodes (Refs. 32, 34, and 35), which is not the case in the present work. Moreover, for the problem we are studying, changes in the functional to include corrections to the SIE will basically change the particular position of the Ni-related resonances but will not modify in a qualitative way our conclusions.

[32] M. Koentopp, C. Chang, K. Burke, and R. Car, J. Phys.: Condens. Matter **20**, 083203 (2008).

[33] G. Stefanucci, S. Kurth, E. K. U. Gross, and A. Rubio, in *Molecular and Nanoelectronics: Analysis, Design, and Simulation*, Elsevier Series on Theoretical and Computational Chemistry, edited by J. Seminario, (Elsevier, New York, 2007), Vol. 17, p. 247.

[34] C. Toher and S. Sanvito, Phys. Rev. B **77**, 155402 (2008).

[35] S.-H. Ke, H. U. Baranger, and W. Yang, J. Chem. Phys. **126**, 201102 (2007).

[36] F. D. Novaes, A. J. R. Silva, and A. Fazzio, Braz. J. Phys. **36**, 799 (2006).

[37] H. Lee, Y.-W. Son, N. Park, S. Han, and J. Yu, Phys. Rev. B **72**, 174431 (2005).

[38] L. Pisani, J. A. Chan, B. Montanari, and N. M. Harrison, Phys. Rev. B **75**, 064418 (2007).

[39] The particular electronic occupation values, as well as the Ni magnetic moment, may depend on the exchange-correlation potential used. Hybrid functionals, such as B3LYP, tend to increase the transition-metal occupation and magnetization (Refs. 40 and 41). However, once again, we do not expect that the changes will modify the results in a qualitative way.

[40] T. Bredow and A. R. Gerson, Phys. Rev. B **61**, 5194 (2000).

[41] M. Marsman, J. Paier, A. Stroppa, and G. Kresse, J. Phys.: Condens. Matter **20**, 064201 (2008).

[42] I. Zanella, S. B. Fagan, R. Mota, and A. Fazzio, J. Phys. Chem. C **112**, 9163 (2008).

[43] H. J. Choi, J. Ihm, S. G. Louie, and M. L. Cohen, Phys. Rev. Lett. **84**, 2917 (2000).

[44] M. V. Fernández-Serra, C. Adessi, and X. Blase, Nano Lett. **6**, 2674 (2006).

[45] M. V. Fernández-Serra, C. Adessi, and X. Blase, Phys. Rev. Lett. **96**, 166805 (2006).

[46] A. R. Rocha, J. E. Padilha, A. Fazzio, and A. J. R. da Silva, Phys. Rev. B **77**, 153406 (2008).